ADVANCED FUNCTIONAL MATERIALS
www.afm-journal.de

Highly Luminous Scintillating Nanocomposites Enable Ultrafast Time Coincidence Resolution for γ-rays Detection with Heterostructured Multilayer Scintillators

Matteo Sala, Matteo Orfano, Valeria Secchi, Ilaria Mattei, Nicolò Pianta, Vojtech Zabloudil, Carsten Lowis, Romana Kučerková, Martin Nikl, Francesco Meinardi, Etiennette Auffray, Irene Villa, and Angelo Monguzzi**

Brighter fast scintillators are needed for advanced applications to acquire data with high signal-to-noise ratio in short time windows, like in the time-of-flight positron emission tomography (ToF-PET) imaging technique for cancer. A new composite polymeric fast scintillator loaded with high-density hafnium dioxide (HfO_2, hafnia) nanoparticles is developed here to be used for detection of the 511 keV γ-rays employed in ToF-PET. By a fine tuning and engineering of the electronic properties of its components, namely the polymeric matrix, the dense nanoparticles and the embedded fluorescent dye, a highly luminous polymeric scintillating nanocomposite is realized, showing an unprecedented scintillation efficiency for plastic materials and nanosecond-scaled scintillation decay. Nanocomposite films are then coupled to dense bismuth germanate ($Bi_4Ge_3O_{12}$, BGO) crystal sheets to fabricate an heterostructured multilayer scintillator as a prototype pixel for ToF-PET scanners. Thanks to the nanocomposite high scintillation efficiency, the prototype detector shows an ultrafast time resolution of 115 ps for 511 keV γ-rays detection, actually limited by the non-optimal light transport properties in the pixel and by the sensitivity of the employed photodetector.

1. Introduction

Faster and brighter scintillators are now requested for several advanced applications where is pivotal to acquire data with high signal-to-noise ratio in extremely short time windows. For example, to detect events avoiding pile up in high energy physics experiments where extremely high event rates are generated,[1,2] or to quickly acquire high quality images at low dose in medical applications as in the ToF-PET cancer imaging technique, where tents of picoseconds time resolutions are desired.[3] A limited coincidence time resolution (*CTR*) is indeed one of the most critical issue to overcome to develop higher efficiency, higher sensitivity and lower dose-working ToF-PET machines. The scanner performance is indeed ultimately set by the detector capability to discriminate in time the arrival of the 511 keV, back-to-back γ-photons pairs generated by the radiotracers injected in the patient body to image the tissues.[1a] In particular, the uncertainty Δx on the annihilation event position is given by $\Delta x = c\ \Delta t = c\ (t_2 - t_1)$ where c is the speed of light in vacuum and t_1, t_2 are the different detection times of the γ-photons on both detectors along the detector line of response.[2] The full width half maximum (FWHM) of the distribution in the recorded Δt is what we call *CTR*. Actually, there are no monolithic scintillating materials which can afford the desired $CTR << 200$ ps, i.e., the current best value for commercial scanners, that would allow millimeter scale imaging resolution with significantly shorter acquisition times and significantly lower and safer radiotracer doses.[3d]

M. Sala, M. Orfano, V. Secchi, N. Pianta, F. Meinardi, I. Villa, A. Monguzzi
Dipartimento di Scienza dei Materiali
Università degli Studi Milano-Bicocca
via R. Cozzi 55, Milano 20125, Italy
E-mail: irene.villa@unimib.it; angelo.monguzzi@unimib.it

The ORCID identification number(s) for the author(s) of this article can be found under https://doi.org/10.1002/adfm.202421434

DOI: 10.1002/adfm.202421434

V. Secchi, A. Monguzzi
NANOMIB
Center for Biomedical Nanomedicine
University of Milano-Bicocca
Milano 20126, Italy

I. Mattei
INFN Sezione di Milano
via G. Celoria 16, Milano 20133, Italy

V. Zabloudil, C. Lowis, E. Auffray
CERN
Espl. des Particules, Geneva 1/1211, Switzerland

R. Kučerková, M. Nikl
FZU - Institute of Physics of the Czech Academy of Sciences
Cukrovarnická 10/112, Prague 16 200, Czech Republic

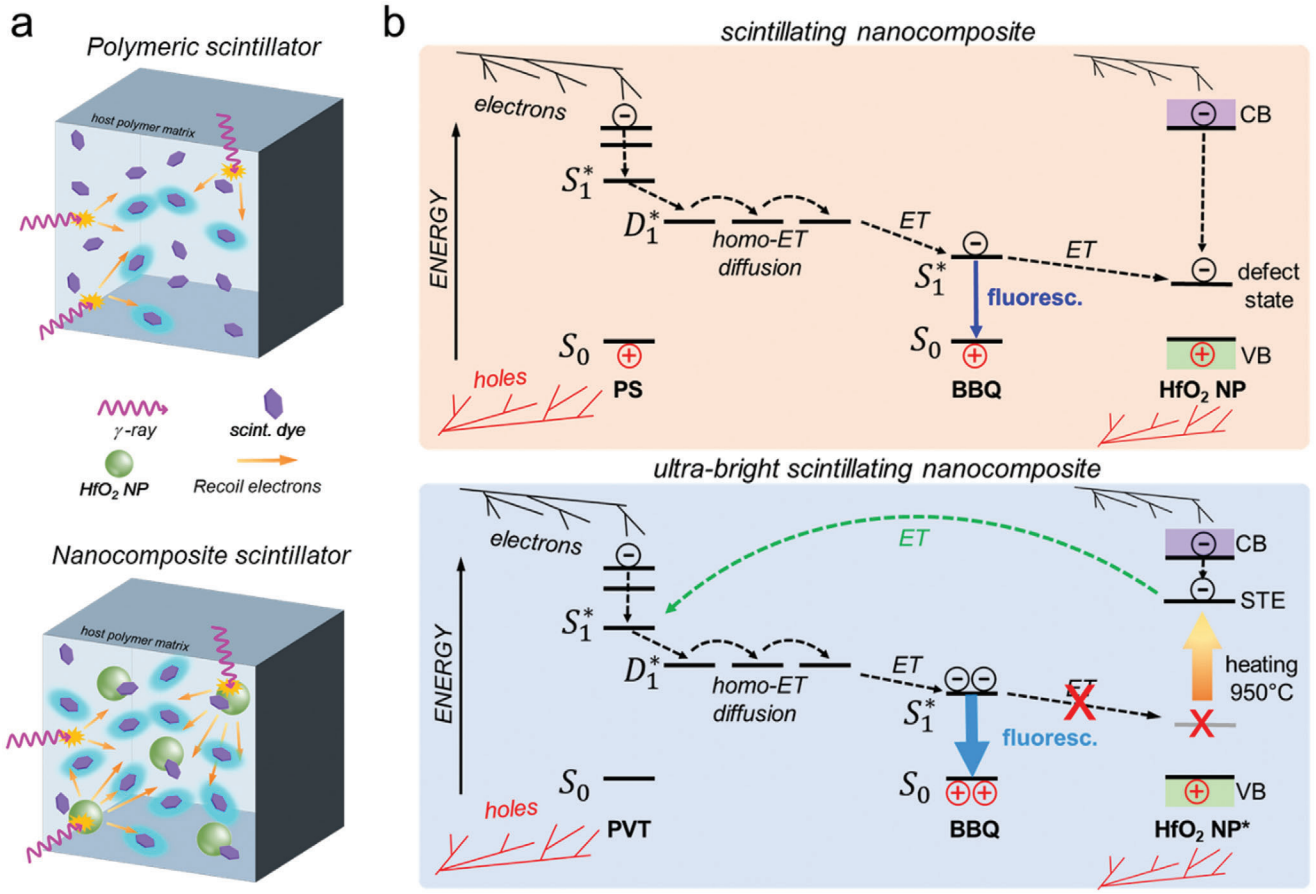

Figure 1. a) Sketch of the scintillation mechanism in composite polymeric materials loaded with dense HfO_2 nanoparticles (NPs). The γ-rays interacts not only with the polymeric, low density host matrix, but also with the NPs, activating a more efficient and localized production of secondary events and free charges that enhances the material scintillation efficiency. b) Simplified outline of the photophysics involved of the scintillation process in standard (top) and ultra-bright (bottom) scintillating nanocomposites. Dashed arrows indicate non-radiative processes. In the standard composite, the diffusing hot charges produced by interaction of γ-rays with the host polymer polystyrene (PS) or NPs quickly recombine to form PS singlet state S_1^*. These states, immediately, form an excimeric state D_1^* with ground state PS. The energy travels within the matrix by homo-molecular energy transfer (ET), through with this states until it is transferred to the embedded emitting dye BBQ, thus promoting it from the ground state S_0 to its fluorescent emissive excited singlet state S_1^*. NPs have a wide energy gap between the valence and conduction bands (VB and CB, respectively) but possess low energy defect states that acts as energy traps for a fraction of diffusing charges and as quenching center for the BBQ luminescence. In the ultra-bright nanocomposite, the employed host matrix is polyvinyl toluene (PVT). NPs have been thermally treated at 950 °C (NP^*s) to eliminate the low energy electronic defects, thus avoiding the quenching of BBQ luminescence molecules and enabling the ET of the energy trapped in the NP^*s self-trapped exciton state (STE) into the PVT matrix.

The concept of multicomponent heterostructured scintillator would enable to surpass this limit.[4] An heterostructured scintillator can be fabricated by mechanically coupling dense scintillating crystals such as BGO to fast-emitting scintillators in different architectures.[4b,5] The dense component stops the γ-rays by means of the photoelectric effect, thus enabling the selection of the correct events at 511 keV. The fast emission is activated both directly by weak direct interaction with the ionizing radiation and, most importantly, by the diffusing recoil photoelectrons generated in the dense component that reach the fast material. This mechanism of energy sharing is actually considered one of the best strategy to obtain simultaneously the energy resolution and the *CTR* required to boost both the quality and the speed of the ToF-PET image reconstruction.[4c]

Candidates as the fast emitter are conjugated fluorescent systems but, unfortunately, scintillating conjugated organic molecules, crystals and polymers are light materials with densities $\rho \approx 1$ g cm^{-3}. The presence of the fast emitter decreases therefore the global density of the multicomponent scintillator and consequently its stopping power at 511 keV.[6] More importantly, their scintillation light yield (LY), defined as the ratio between the number of emitted photons and the energy deposited in the system, is usually assessed below 20000 ph MeV^{-1} for commercially available materials.[7] These characteristics limit the absolute scintillation light output and consequently the detector sensitivity, especially in the case where small device as the ToF-PET scanners pixels are required. To mitigate these issues, the use of hybrid organic/inorganic compounds[8] or the loading of polymeric hosts with optically inert dense nanoparticles (**Figure 1a**) has been recently proposed.[9] The presence of dense nanoparticles including elements with high atomic number Z affects indeed both the Compton and the photoelectric interactions

probability with high energy photons,[10] which increase with the effective material electronic density, i.e.the effective Z value. Besides, and importantly, even at low nanoparticles concentration where the average density of the material does not change we observe a clear enhancement of the material LY, because of a peculiar effect due to the locally enhanced density of free charges generated around nanoparticles upon radiation/matter interaction that favors their recombination to emissive states.[11]

Here we developed a highly luminous composite polymeric fast scintillator loaded with high-density hafnia nanoparticles to be used as the fast emitter in the multilayer scintillator architecture. By finely engineering and maching the electronic properties of the system components, namely the host matrix, the heavy nanoparticles and the fluorescent dye used as final emitter, we improve the yield of charges recombination in the host matrix and the efficiency of the energy transfer from the host to embedded chromophores, thus realizing an extremely luminous polymeric nanocomposite scintillator that surpasses any commercial plastic material (Figure 1a). In the best composition we employ polyvinyltoluene as the host matrix for the fast emitting dye 4,4‴-bis[(2-butyloctyl)oxy]-1,1′:4′,1″:4″,1‴-quaterphenyl (BBQ). Thermally treated hafnia nanoparticles, with their density of $\rho = 9.68$ g cm^{-3}, are the radiosensitizers.[12] The system's properties have been fully investigated by steady state and time resolved photoluminescence and scintillation spectroscopy. The nanocomposite shows a remarkable light yield LY ≈60 000 ph MeV^{-1} under soft X-rays and a fast scintillation kinetics with ≈0.12 and ≈2 ns of rise and decay time, respectively. We fabricated a series of 100 µm-thick nanocomposite films to be coupled to 100 µm BGO crystalline sheets, thus realizing a short multilayer scintillator ($3 \times 3 \times 3$ mm^3) as prototype detection pixel for ToF-PET scanners that upon interaction with 511 keV γ-rays shows an ultrafast CTR of 115 ps.[13]

2. Fabrication and Engineering of Scintillating Nanocomposites

To realize highly emissive composites, we employ here the BBQ dye as the final emitter instead of the previously used POPOP[4b] because it has an excellent photoluminescence quantum yield $\phi_{pl} = 0.93$ in the spectral region where scintillator photodetectors work at best, a faster emission lifetime of 0.7 ns (**Figure 2a**; Figure S1, Supporting Information)[14] and a better solubility in the reference host polymer polystyrene (C_8H_8, $\rho = 1.06$ g cm^{-3}). Figure 1b outlines the main mechanisms involved in the investigated scintillation process, where the diffusing free hot charges produced by the interaction of ionizing radiation with the polymer matrix recombine to generate the emissive states that produces the scintillation light pulses. Notably, the highest occupied and lowest unoccupied molecular orbital energies are similar for POPOP and BBQ (Figures S2–S4, Supporting Information), so we assume they have the same charge capture ability. Moreover, the BBQ absorption spectrum is more resonant with the UV emission of the polystyrene excimers promptly formed during the scintillation process than the one of POPOP, thus enhancing the speed and maximizing the yield of the host-to-dye energy transfer that activates the dye near UV-blue fluorescence (Figure 2a).[11,15] Figure 2b shows the radioluminescence spectra of a polystyrene-based scintillators series with different loading levels of BBQ from 10^{-5} M to 10^{-1} M, under soft X-rays excitation (Experimental Section). Following the increasing BBQ amount, we observe a reduction of the polystyrene emission intensity and lifetime (Figure 2c), with a simultaneous increment of the BBQ luminescence intensity activated by the progressively more efficient non-radiative energy transfer from the polymer matrix. A slight redshift in the BBQ luminescence spectrum can be noticed at highest concentration employed, due to trivial self-absorption of emitted light. The polystyrene-to-BBQ energy transfer reaches a unitary yield using 10^{-1} M of BBQ, with a rate of 11.5 GHz (Figure S5, Supporting Information). This composition shows a LY = 3800 ± 200 ph MeV^{-1} under soft X-rays (Figure 2g,i, Experimental Section).

This best polystyrene-based scintillator containing 10^{-1}M BBQ molecules (PS:BBQ) has been therefore tentatively improved by adding different relative weight loading of oval crystalline hafnia nanoparticles (NPs-wt.%) of size ≈75 nm along the long axis and 33 nm for the short axis (Figure 2d left panel, Figure 2e; Figure S6, Supporting Information). The aim was to find the composition that maximizes the nanoparticle's radiosensitization effect partially compensating the Onsager losses typical of low density polymeric scintillators, as previously observed.[4b,16] Surprisingly, the series LY monotonically decreases with the nanoparticles amount down to 1800 ph MeV^{-1} for the sample with 4.0 ± 0.2%wt. of loading (PS:BBQ:NP-4%, Figure 2g,i). We ascribe this effect to the larger optical gap of BBQ with respect to POPOP. The weak radioluminescence spectrum of nanoparticles is indeed peaked at ≈425 nm (2.92 eV) extending down to 600 nm (Figure 2f). This emission is not due to their inter-band recombination, whose energy lies in the UV spectrum at ≈5–6 eV,[17,18,19] but it is due to inefficient radiative recombination of low energy intra-gap defect states.[20,21,22] Given that the BBQ emission is peaked at 3.02 eV (410 nm), and therefore higher than the one of nanoparticles defects, the BBQ-to-defects energy transfer is an active quenching pathway, as demonstrated by the concentration-dependent results on the BBQ emission lifetime that show how nanoparticles act as quenchers for the dye luminescence (Figure S7, Supporting Information). This finding also suggests that the energy of diffusing charges that directly recombine on nanoparticles defects is lost. Notably, the direct recombination of charges on nanoparticles is a probable pathway due to the high loading levels required to maximize the radiosensitization (Figure S3, Supporting Information). Thus, both these mechanisms limit the system global yield (Figure 1b, top).

To overcome this issue, we performed a thermal annealing treatment on nanoparticles by heating them at 950 °C (Experimental Section). The high temperature improves the system crystallinity (Figure 2e) and gives to nanoparticles a more defined spherical profile with 43 nm diameter, clearly observed with electronic microscopy (Figure 2d right; Figure S6, Supporting Information).[23] A higher crystallinityis usually accompanied by a reduction of low energy intra-gap levels related to structural disorder and defects.[24] Indeed, the radioluminescence spectrum of annealed nanoparticles largely shifts toward the UV region, with the appearance of a 250 nm (4.96 eV) emission assigned to the hafnia self-trapped exciton (Figure 2f).[25,26] Notably, this energy is higher that the polystyrene optical gap at 280 nm (4.42 eV). This suggests that the energy of charges that recombine on nanoparticles can be injected again in the host matrix by non-radiative

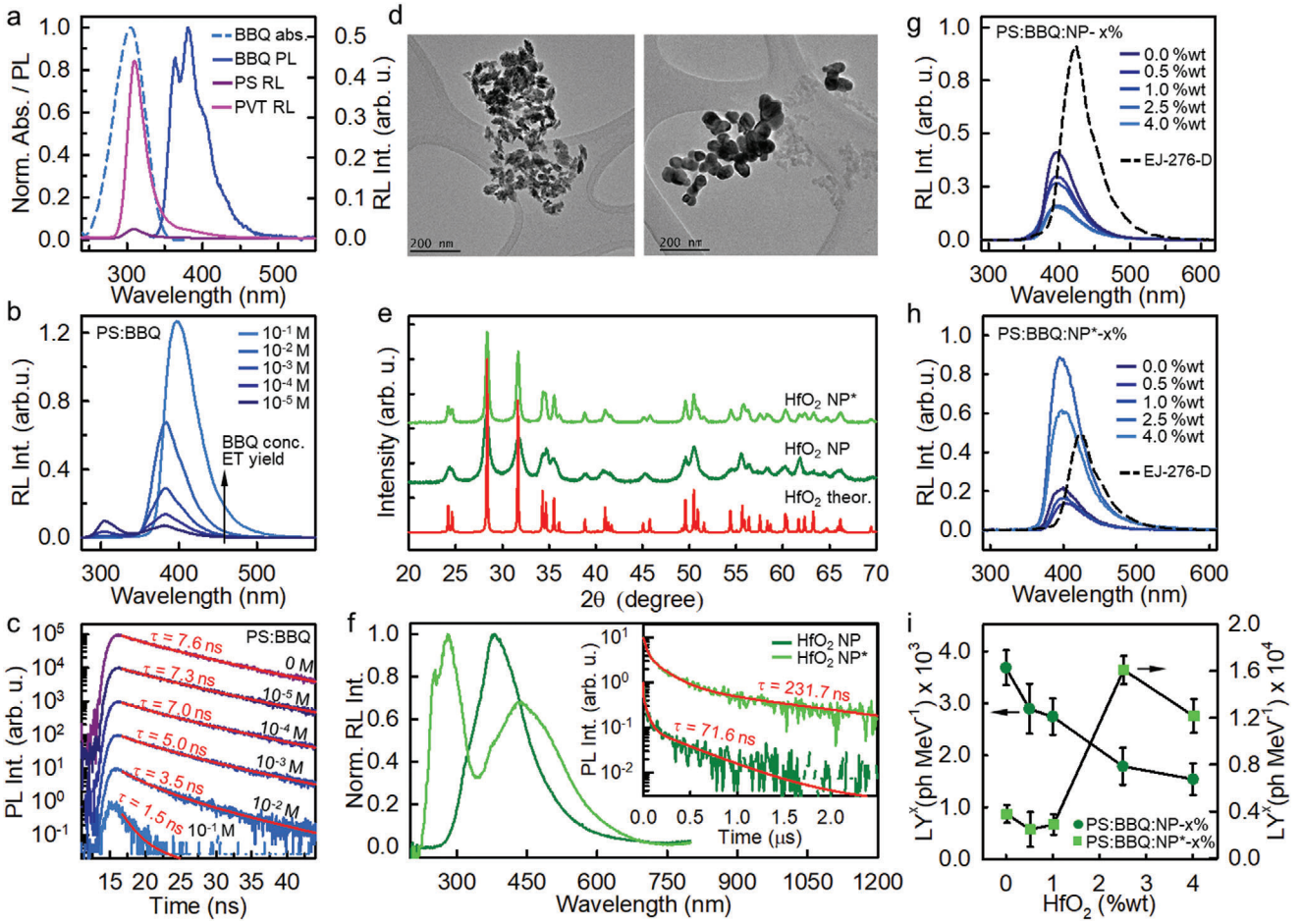

Figure 2. a) Optical absorption and photoluminescence (PL) of BBQ in a 10^{-5} M cyclohexane solution under 340 nm excitation. Radioluminescence (RL) spectra of polystyrene (PS) and polyvinyl toluene (PVT) under soft X-rays. b) RL spectra of the PS:BBQ polymeric scintillators series as a function of the BBQ molar concentration under soft X-rays. c) PL intensity decay in time recorded at 320 nm for the PS:BBQ polymeric scintillators series under pulsed excitation at 250 nm. Solid lines are the fit of data with single- or multi-exponential decay functions. d) Transmission electron microscope (TEM) images of HfO_2 nanoparticles pre- (NP) and post- (NP*) thermal treatment at 950 °C. e) Theoretical and experimental XRD powder spectrum of monoclinic HfO_2, NPs and NP*. f) RL spectra of NP and NP* powders under soft X-rays. The inset is the powders PL decay time at 380 nm under pulsed laser excitation at 250 nm. Solid lines are the fit of data with single- or multi-exponential decay functions. g) RL spectra of the PS:BBQ:NP-x% composite scintillators series as a function of the NP loading in weight fraction (%wt.) under soft X-rays. h) RL spectra of the PS:BBQ:NP*-x% composite scintillators series as a function of the NP loading in weight fraction (%wt.) under soft X-rays. i) Light yield (LY) of the PS:BBQ:NP-x% (circles) and PS:BBQ:NP*-x% (squares) composite scintillators series measured as function of the NP (NP*) loading level in weight fraction (%wt.) under soft X-rays. The RL spectrum of the commercial EJ-276-D plastic scintillators recorded under the same experimental conditions is reported for reference.

energy transfer (Figure 1b, bottom). Moreover, the partial elimination of hafnia's low energy defects makes negligible the competitive energy transfer from excited BBQ molecules to nanoparticles (Figure S8, Supporting Information). The effectiveness of this approach to improve the material light output is clearly demonstrated by looking at radioluminescence intensity of the new series of nanocomposites reported in Figure 2h. Here we observe the expected non-monotonic behavior of the emission intensity versus nanoparticles loading.[11,16] A maximum LY = 16 500 ± 900 ph MeV^{-1} under soft X-rays is achieved with a loading of 2.5 ± 0.2%. Notably, this value is +50% higher than the one obtained with POPOP, most probably due to the larger resonance between the host emission and the BBQ absorption which increase the non-radiative transfer rate and yield from polystyrene excimers to embedded dyes thus reducing the effectiveness of competitive non-radiative energy loss pathways in the matrix.

Once improved the interplay between nanoparticles and fluorescent dyes, we further enhanced the nanocomposites scintillation performance by using a different host matrix, namely the polyvinyltoluene (C_9H_{10}, ρ = 1.03 g cm^{-3}). This latter is a preferred choice here because it has the same chemical and structural properties of polystyrene, but it shows one order of magnitude more intense radioluminescence while keepingsimilar spectral properties (Figure 2a). This suggests a more efficient conversion of diffusing free charges into the polymer excimeric emissive states (Figure 1b) that should results a larger scintillation yield. **Figure** 3a shows the radioluminescence spectra of a polyvinyltoluene:BBQ composite scintillators series (PVT:BBQ:NP*-x%) measured as a function of the nanoparticles

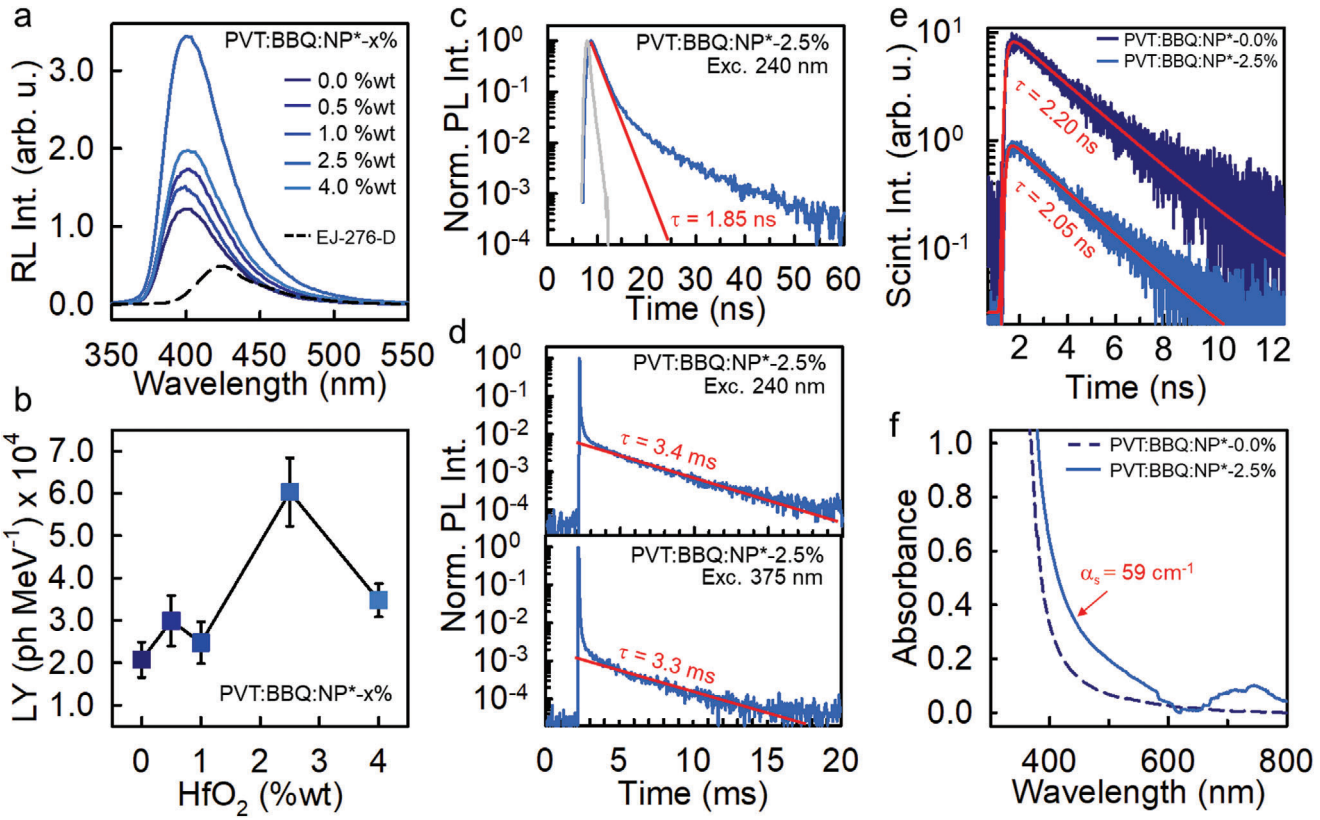

Figure 3. a) RL spectra of the PVT:BBQ:NP-x% composite scintillators series as a function of the NP loading in weight fraction (%wt) under soft X-rays. b) Light yield of PVT:BBQ:NP*-x% (squares) composite scintillators series as function of the NP* loading level in weight fraction (%wt). c,d) Time-resolved photoluminescence (PL) spectra of the PVT:BBQ:NP*-2.5% composite scintillator under pulsed laser excitation at 250 nm (120 ps pulse width) in the c) nanosecond and d) millisecond time range at 400 nm. Solid lines are the fit of data with multi-exponential decay functions. e) Scintillation pulse at 400 nm from the PVT:BBQ:NP*-2.5% composite scintillators and the PVT:BBQ polymeric scintillator 100 μm-thick films under pulsed X-rays excitation (14.5 keV, 120 ps pulse width). Solid lines are the fit of data with single exponential decay functions. f) Optical absorption spectra of the PVT:BBQ:NP*-2.5% composite scintillators and the PVT:BBQ polymeric scintillator (100 μm films at normal incidence). The apparent absorption at 430 correspond to scattering coefficient as a large as $\alpha_s = 59$ cm^{-1}.

loading level under soft X-rays. We observe again the same non-monotonic incremental behavior and, notably, we achieve a LY as large as = 63 500 ± 5000 ph MeV^{-1} for the PVT:BBQ:NP*−2.5% sample (Figure 3b; Figures S9 and S10, Supporting Information), by far larger than the one of any commercial polymeric scintillator and several inorganic crystals., i.e., the BGO. Time resolved photoluminescence spectroscopy experiments allow to better understand the properties of the ultra-bright scintillating nanocomposite. Figure 3c shows its transient photoluminescence spectrum recorded 410 nm under pulsed excitation at 240 nm (Experimental Section). The emission intensity decays with a multi-exponential behavior. Beside the evident prompt emission in a short time of $\tau = 1.85$ ns, there is a slower component that spans up to the millisecond time range (Figure 3d). This finding suggests a possible involvement of the triplet states of the conjugated moieties in the generation of scintillation light. Interestingly, the relative intensity of the photoluminescence slow component changes according to the excitation energy. In particular, the slow emission is more intense when the host polymer is excited at 240 nm (Figure 3d top, ca. 50% of the total emission) with respect when the BBQ molecules are directly excited at 375 nm (Figure 3d bottom, ca.5% of the total emission). A detailed picture of the mechanism involved is difficult to point out, however these findings suggest that the high-energy, optically dark polyvinyltoluene triplets can be involved in the scintillation process to generate BBQ emissive states when formed by diffusing charge recombination.[27,28] For example, an efficient interaction can be envisaged considering the resonance with BBQ absorption and the proximity (<2 nm) of conjugate units in the host polymer and the embedded dyes, which can enable dipole-forbidden and spin-forbidden transitions through non radiative energy transfer processes between the two species. However, the long-time emission completely disappear upon ionizing radiation, so further studies are still ongoing to understand this intriguing interplay between the polymeric host and the guest dyes during scintillation.[4b]

The nanocomposite has been successively prepared as a film of 100 μm thickness, in order to be coupled and piled up with 100 μm BGO sheets to fabricate a multilayer scintillator (see Section 3). As showed in Figure 3e, the scintillation light pulses generated in the film at 410 nm under pulsed X-rays excitation shows a mainly single exponential fast decay time of $\tau = 2.05$ ns $= \tau_{d,eff}^{nanoc.}$, and a rise time of $\tau_{rise}^{0} = 123$ ps (Figure S11, Supporting Information). No substantial differences in the scintillation kinetics can

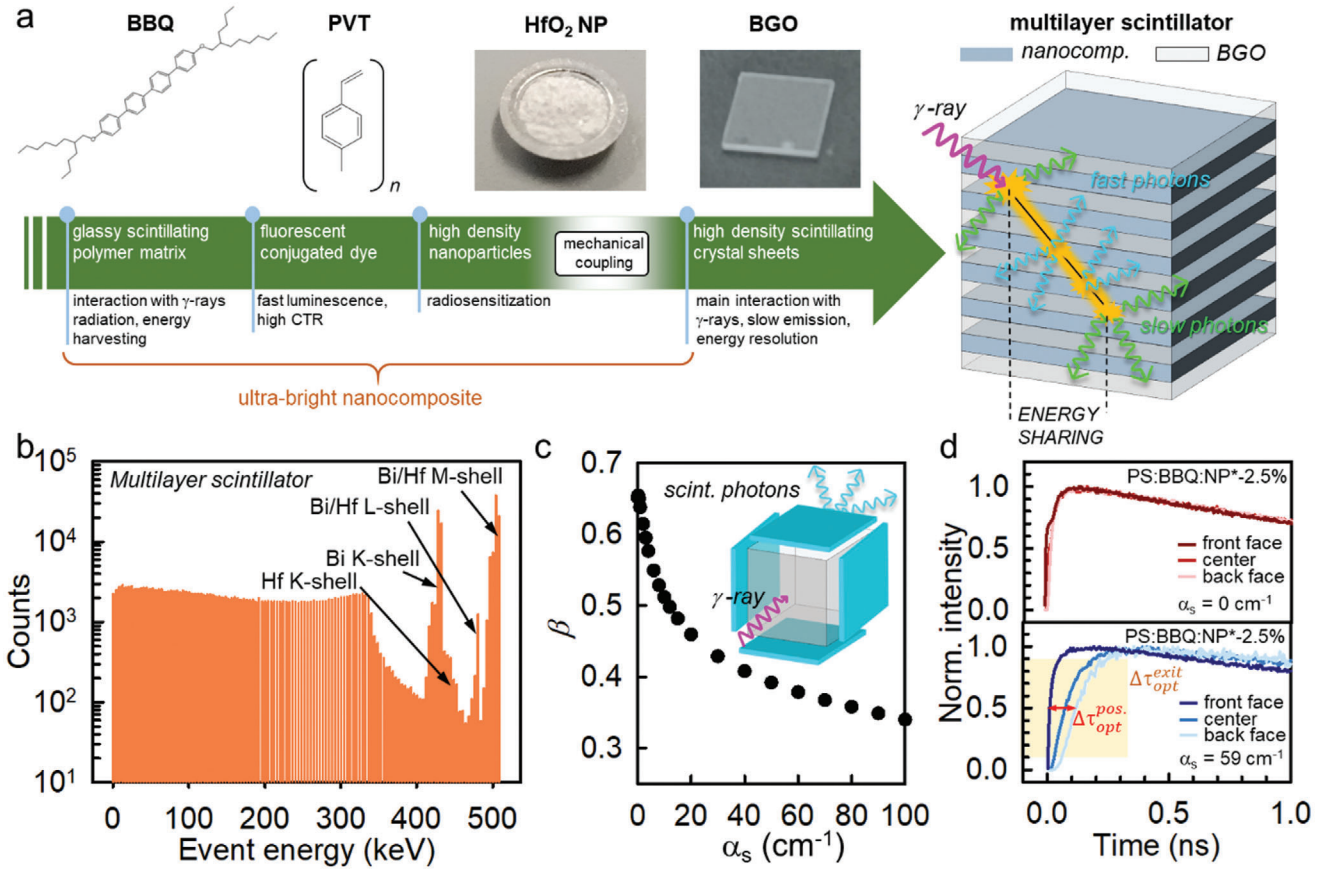

Figure 4. a) Sketch of the ultra-bright nanocomposite constituents and the manufacturing procedure for the multilayer scintillator. b) Energy loss events probability calculated by a Monte Carlo simulation for $3 \times 3 \times 3$ mm^3 multilayer scintillator composed of alternating 100 µm layer of PVT:BBQ:NP*-2.5% and BGO for 511 keV γ-rays. c) Light outcoupling efficiency β (dots) calculated as a function of the scattering level (α_s) for a $3 \times 3 \times 3$ mm^3 cube of pure PVT:BBQ:NP*-2.5% composite with 4 mirrors put on the lateral surfaces (inset). The diamond shows the experimental β value obtained from *CTR* measurements. d) Scintillation pulse calculated without (top, $\alpha_s = 0$ cm^{-1}) and with experimental scattering (bottom, $\alpha_s = 59$ cm^{-1}) for the same nanocomposite cube as a function of the scintillation event position, respectively at the input face (front face), in the cube center (center) or at the output face (back face). The double headed arrow marks the maximum uncertainty $\tau_{opt}^{pos.}$ calculated at 50% of the pulse rise due to different events position in the sample. The shaded area outline the slowdown of the pulse rise time that enable to estimate the maximum uncertainty τ_{opt}^{exit} on the scintillation photons exit time due to scattering that modify their optical paths.

be observed in absence of nanoparticles, thus demonstrating that they do not affect the material time response, and no afterglow can be detected (Figure S12, Supporting Information). However, the presence of nanoparticles affects the optical and light transport properties of the scintillator, which shows a more evident scattering background in the optical absorption spectrum with respect to the nanoparticles-free sample (Figure 3f).

3. Radiation Matter Interaction, Light Transport, and Scintillator Time Response

The multilayer scintillator has been realized by duplicating a single mechanically-coupled nanocomposite/BGO heterostructure (100 µm/100 µm) to reach a final size of $3 \times 3 \times 3$ mm^3 (Experimental Section). As sketched in **Figure** 4a, incident γ-rays activate the multilayer scintillator luminescence by photoelectric effect in BGO or through energy sharing between BGO and the fast-emitting nanocomposite. The device *CTR* can be estimated from several parameters intrinsic of the employed materials by

$$CTR = 3.33\sqrt{\frac{\tau_{rise}\tau_{d,eff}}{N}} \quad (1)$$

The parameter $\tau_{rise} = 1.57\tau_{rise}^{0} + 1.15\tau_{opt}$ is the total rise time of the scintillation pulse, which is given the sum of the intrinsic scintillation rise time τ_{rise}^{0} of the scintillator and the average spread of the optical photons transit time to the photodetector τ_{opt}.[29] The effective emission decay time $\tau_{d,eff} = (k_{dtc})^{-1}$ is calculated as the reciprocal of the detection rate of scintillation photons k_{dtc} (Section S5, Supporting Information) and N is the number of photons collected by the photodetector. Considering a multicomponent scintillator where the building block materials show different LY values and scintillation kinetics, in order to take into account these aspects Equation (1) can be evolved to

$$CTR = 3.33 \sum_i A_i \sqrt{\frac{\tau_{rise}\tau^i_{d,eff}}{\beta\ \chi\ \mathrm{LY}^i_{\mathrm{eff}} E}} \quad (2)$$

At the denominator, the N value is now expressed as a function of several parameters characteristic of the considered scintillators, including the amount of energy deposited $E = 511$ keV and the effective total yield $\mathrm{LY}^i_{\mathrm{eff}} = \epsilon_i \mathrm{LY}_{\mathrm{nanoc.}} + (1-\epsilon_i)\mathrm{LY}_{\mathrm{BGO}}$, where ϵ_i is the fraction of energy deposited in the nanocomposite for i-event E_i / 511 keV (Experimental Section). The BGO shows a $\mathrm{LY}_{\mathrm{BGO}} = 10\ 000$ ph MeV^{-1}. The light outcoupling efficiency β marks the fraction of scintillation photons that reach the photodetector, and χ represents the photodetector quantum efficiency. For the nanocomposite we measured under γ-rays its scintillation light output $\phi_{scint} = \beta_{nanoc.}\mathrm{LY}_{nanoc.}$, from which we derived a $\beta_{nanoc.} \approx 0.05$ (Section S7, Supporting Information), in agreement with the poor material transparency (Figure S10, Supporting Information). This value is two order of magnitude lower than the theoretical $\beta = 0.65$ calculated considering re-absorption effects, ideal interfaces, and mirrors with 95% reflectivity around the device and a null scattering coefficient $\alpha_s = 0$ cm^{-1}, but also lower than the expected theoretical value of $\beta_{th} = 0.38$ calculated accounting for the effective photon scattering with $\alpha_s = 59$ cm^{-1} (Figure 4c).

At the numerator, the scintillator effective global scintillation decay time $\tau_{d,eff}$ can be represented as a linear combination of all the possible $\tau^i_{d,eff}$ for each i-shared event. The single $\tau^i_{d,eff}$ value depends therefore on the effective scintillation decay time in the composite ($\tau^{nanoc.}_{d,eff}$) and in the BGO ($\tau^{BGO}_{d,eff}$) by

$$\tau^i_{d,eff} = \left[\frac{\epsilon_i\theta}{\tau^{nanoc.}_{d,eff}} + \frac{(1-\epsilon_i)(1-\theta)}{\tau^{BGO}_{d,eff}}\right]^{-1} \quad (3)$$

The $\tau^i_{d,eff}$ contribution in Equation (1) is weighted by the distribution of probability A_i that the i-shared event deposits in the nanocomposite a fraction ϵ_i of the BGO photoelectric recoil electrons energy producing photons with a relative yield $\theta = \mathrm{LY}_{\mathrm{nanoc.}}/\mathrm{LY}_{\mathrm{tot}}$. By directly measuring the properties of the individual materials, it is therefore possible to model the device theoretical best CTR with good accuracy through Equation (2).[30]

Figure 4b reports the energy loss events probability calculated by a Monte Carlo simulation for the multilayer scintillator exposed to 511 keV γ-rays, which has been designed and run to evaluate the global behavior of the device (Experimental Section, Section S7, Supporting Information). Besides the usual Compton shoulder at low energies, above 400 keV we can distinguish three different photoelectric peaks at ≈440, 475, and 509 keV, respectively. These are the photoelectric events originating upon partial absorption of γ-rays from the K-shell (77–90 keV), L-shell (9–16 keV), and M-shell (2–2.5 keV) electrons of Bi and Hf in the BGO and nanocomposite layers, respectively.[31] This statistical modeling enables to specifically calculate the A_i, E_i and ϵ_i values necessary to estimate the system time response by combining Equations (2) and (3). Considering the device size and a scattering coefficient $\alpha_s = 59$ cm^{-1} at 410 nm (Figure 3f, Experimental Section), we have a $\tau_{opt} = 227$ ps given by the distribution of photons' optical paths before detection.[32] Specifically, the $\tau_{opt} = \Delta\tau^{pos.}_{opt} + \Delta\tau^{exit}_{opt}$ value has been calculated as the sum of two contributions (Figure 4d). The first is the maximum uncertainty $\Delta\tau^{pos.}_{opt} \approx 100$ ps calculated at 50% of the pulse maximum intensity, due to the different positions of scintillation events in the sample. The second term $\tau^{exit}_{opt} \approx 127$ ps is the maximum uncertainty on the photons exit time, due to the sample scattering that modify their optical path before reaching the photodetector. In this case, the combination of the experimental τ^0_{rise} and of the simulated τ_{opt} results an effective total $\tau_{rise} = 450$ ps for the device. Therefore, given that the BGO and the nanocomposite film shows a $\tau^{BGO}_{eff} = 97.9$ ns and $\tau^{nanoc}_{eff} = 2.02$ ns, respectively,[33] a theoretical best-time response $CTR_{th} = 71$ ps is estimated considering the certified $\chi = 0.25$ at 410 nm for the photodetector (Figure S15, Supporting Information) and the ideal $\beta_{th.} = 0.38$ for the selected experiment configuration (Experimental Section, Figure 4c).[32]

We therefore tested the multilayer scintillator under operative conditions. **Figure 5** depicts the time-integrated pulse height spectra recorded under exposition to 511 keV γ-rays (Experimental Section). For reference, we measured the scintillation of a 3 × 3 × 3 mm^3 cube of pure PVT:BBQ:NP*-2.5% composite (Figure 5a) and BGO (Figure S13, Supporting Information). Since the nanocomposite and BGO have very different emission lifetimes, the scintillation pulses of events depositing energy in one or the other material are clearly different, thus allowing a pulse shape discrimination (Figure 5b).[34] The multilayer scintillator shows a complex behavior, with a spectrum that contains three regions of interest where the scintillation events are occurring solely in BGO, solely in the fast nanocomposite and where we can find the shared events. This demonstrates that the recorded output signal is generated by an effective interaction between the device components. According to Monte Carlo simulations of the radiation/matter interaction in the system (Experimental Section),[35] the average fraction of useful events with energy loss > 440 keV in the results as high as a respectful 28% versus the 38% of monolithic BGO of the same size (Figure S13 and Tables S2–S4, Supporting Information). A detailed data analysis allows us to distinguish the events useful for imaging reconstruction, that is, the fast light pulses generated in the nanocomposite by recombination of the recoil electrons produced solely by the photoelectric effect in the BGO. As shown in Figure 5c, a change in coordinates from [time-integrated signal versus amplitude] to [energy in BGO versus energy in nanocomposite] enable to select the useful shared events. First, we must consider the photoelectric peak corresponding to events fully contained in BGO that release 511 keV of energy deposited in BGO and 0 keV the nanocomposite. At this point, the distribution of events where 0 keV are deposited in BGO and 511 keV in the nanocomposite is reconstructed.[30] By knowing these two points, the energy calibration of the SiPM photodetector employed can be performed (Experimental Section). The straight lines in Figure 5c mark the region where we find the events where the total energy deposited in the device lies between 440 and 665 keV, i.e., the events useful for imaging, and at least 50 keV are shared in the nanocomposite. This specific energy window is the default setting employed in operating instrumentation enabling the best image reconstruction in ToF mode, which is taken here as a reference operating condition.[5c,36] Figure 5d reports the results of the CTR measurements obtained using these operational settings. The CTR is

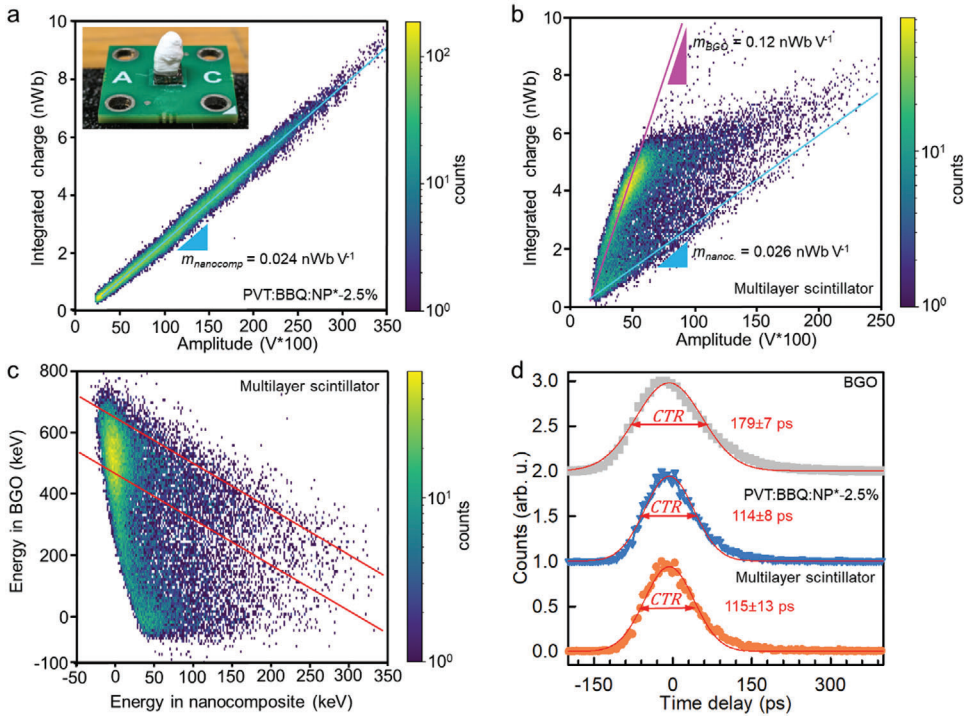

Figure 5. a) Time-integrated pulse-height spectra of monolithic 3 × 3 × 3 mm^3 PVT:BBQ:NP*-2.5% nanocomposite cube. The inset is digital picture of the cube wrapped in Teflon and optically coupled to a Broadcom NUV-MT SiPM photodetector. b) Time integrated pulse-height spectrum of 3 × 3 × 3 mm^3 multilayer scintillator made alternating 100 μm layers of BGO and PVT:BBQ:NP*-2.5%. Pink and cyan straight lines are a guide for the eye to highlight the events occurring solely in BGO and nanocomposite, respectively. The area between the straight lines marks the shared scintillation events. c) [energy in BGO] versus [energy in nanocomposite] spectrum of the multilayer scintillator. Straight lines represent the energy threshold values employed to select the shared fast scintillation events that originate from BGO photoelectric recoil electrons diffusing into the nanocomposite. As photoelectric events, we consider those with total reconstructed deposited energy between 440 to 660 keV. We consider as shared photopeak only the events where at least 50 keV of energy is deposited in the nanocomposite by recoil electrons from BGO. d) Experimental *CTR* of bulk BGO, monolithic PVT:BBQ:NP*-2.5% and multilayer scintillator measured under 511 keV γ-rays excitation.

obtained as the FWHM value of the statistical distribution of the recorded time differences in the detection of 511 keV back-to-back γ-rays emitted by ^{22}Na atoms. Notably, the multilayer scintillator shows a *CTR* as low as 115 ± 13 ps, thus significantly lower than the 179 ± 7 ps of pure BGO and the 180 ps of the previously investigated multilayer scintillator,[4b] and also slightly better than the one obtained using traditional, but transparent, plastic scintillators as fast emitters in the very same architecture.[5c] Notably, the prototype time response matches the one of a reference nanocomposite cube (114 ± 8 ps) but with a significantly stronger stopping power for 511 keV photons due to BGO sheets, thus surpassing the performance of some recently proposed heterostructured scintillators based on heavy scintillating perovskites.[5a] We ascribe this result to the net improvement in the LY achieved[4b] that effectively compensates the poor light extraction observed in the nanocomposite. In this regard, considering that the only free parameter in Equation (1) is the optical coupling factor, we can derive from experimental data the global light transport and extraction properties of the multicomponent device. The observed *CTR* corresponds to an effective light outcoupling yield $\beta_{eff} \approx 0.29$, a value larger than the one of the nanocomposite alone, but still far from the ideal 0.65.[32] This finding suggests that the multilayer architecture helps to extract fast scintillation photons, most probably thanks to the waveguide effect of the transparent BGO sheets and to the reduced effect of scattering in the thin nanocomposite films. However, a significant part of the photons is trapped inside the scintillator. Moreover, the quantum efficiency of the fast photodetector needed here is relatively low at around $\chi = 0.25$ (Figure S15, Supporting Information). Therefore, according to Equation (2), is it straightforward to see that improving the prototype Tof-PET pixel by the use of a photodetector with a better $\chi = 0.5$ would enable to achieve a time resolution of 81 ps, the same recorded in multilayer scintillators where ultrafast emitting semiconductor nanoplatelets are employed.[37] The realization of an heterostructure with maximum light extraction will allow then to improve the device *CTR* down to 54 ps, thus with a real and significant net improvement in the ToF-PET pixel sensitivity.

4. Conclusion

To summarize, by tuning and optimizing the electronic properties of its fundamental building blocks we realized an ultra-bright scintillating and fast emitting nanocomposite. Beside a wise choice of a polymeric host matrix and a fluorescence dye with strictly complementary electronic properties to maximize the host-to-dye energy transfer speed and yield, the key step in the material development was the modification of the electronic

properties of the dense hafnia nanoparticles employed as radiosensitizers with a thermal treatment. The consequent partial elimination of their low-energy electronic defects allowed to maximize the radiosensitization effect in the polymeric host by reducing competitive energy dissipation channels for diffusing charges and optical excitons during scintillation. This allowed to increase the material scintillation yield by a factor ≈400% while keeping its excellent fast time response in the nanoseconds time scale. Thanks to these results, the nanocomposite has been used to fabricate a multilayer scintillator as a prototype for the optical part of a detector suitable for ToF-PET scanners. The device has been realized by alternating films of nanocomposite and crystalline BGO sheets. The latter is the dense material that stops the ionizing radiation activating the energy-sharing mechanism that triggers the fast nanocomposite emission. Upon exposure to 511 keV γ-rays, we observe a synergetic response of the components in the multilayer device. Thanks to the effective activation of the luminous nanocomposite trough energy sharing, we obtained a coincidence time resolution of 115 ps in a pixel prototype, a net improvement with respect to monolithic BGO of same size while preserving approximately 70% of its radiation stopping power. This time response surpasses our previous results and several recently proposed advanced systems, but it is still slower than the best expected theoretical value. The obtained results indicate that an accurate manufacturing is strictly required to improve the optical and light transport properties of the nanocomposite itself and of the heterostructured scintillator to match the ones of bulk crystalline system.[5b] Indeed, considering the scintillation yield achieved, a proper enhancement of light outcoupling must be the focus of future research in order to reach the desired $CTR < 50$ ps required to surpass the low accuracy of dense and slow crystals currently employed in ToF-PET scanners.

5. Experimental Section

Preparation and Structural Characterization of High Crystalline HfO_2 Nanoparticles: The HfO_2 nanoparticles were synthesized by hydrothermal route:[38] the hafnium hydroxide chloride ($Hf(OH)_2Cl_2$) solution was first prepared by dissolving 0.160 g of $HfCl_4$ in 10.0 mL of deionized water. NaOH aqueous solution (3.0 M, 10.0 mL) was added dropwise to the solution above, causing the reaction with $Hf(OH)_2Cl_2$ to form hafnium hydroxide ($Hf(OH)_4$). After that, the solution was transferred into a 100 mL Teflon-lined autoclave and the sealed autoclave was heated to 120 °C and maintained for 24 h. The products were purified by centrifugation for three cycles with alcohol and deionized water alternately after the autoclave was cooled down. Finally, the precipitate was dried at 50 °C for 24 h. The powder was placed in quartz crucible and heated in a muffle oven with a heating rate of 10 °C min^{-1}, the samples were kept at the final temperature of 950 °C for 2 h.[39] The structure and composition of HfO_2 nanoparticles were evaluated by means of powder X-ray diffraction (PXRD) structure and transmission electron microscopy (TEM). Details and data are reported in the Section S4 (Supporting Information). XRD show a well-defined series of diffraction peaks in agreement with the values of monoclinic hafnium dioxide.

Preparation of Nanocomposites: Styrene monomer was purchased from Sigma-Aldrich (CAS no. 100-42-5) under the form of a liquid and colorless monomer. After the removal of stabilizer, the 4,4‴-Bis[(2-butyloctyl)oxy]-1,1′:4′,1″:4″,1‴-quaterphenyl (BBQ, Exciton Luxottica, CAS no. 18434-08-07, MW = 675.01 g mol^{-1}) dye was dissolved with the addition of the as-prepared hafnium oxide NPs. The monomer polymerization followed a thermal pathway by using Azobisisobutyronitrile (AIBN), a free radical initiator, the VAZO 64 (Chemours). The final composition was obtained as follows: 67.5 mg of BBQ and 1 mg of VAZO 64 were dissolved in 1 ml of styrene through ultrasonic stirring. Hafnia NPs were added to the solution, and then dispersed through stirring. The as-prepared solution was placed in a temperature-controlled oil bath at 80 °C for 1 day. For the first 8 h, the mixture was mechanically stirred every hour to avoid nanoparticles sedimentation. Vinyl-toluene monomer was purchased from Sigma-Aldrich (CAS no. 622-97-9) in the form of a liquid and colorless monomer. After the removal of the stabilizer, 4,4‴-Bis[(2-butyloctyl)oxy]-1,1′:4′,1″:4″,1‴-quaterphenyl (BBQ, Exciton Luxottica, CAS no. 18434-08-07, MW = 675.01 g mol^{-1}) dye was dissolved with the addition of the as-prepared hafnium oxide NPs. The monomer polymerization followed a thermal pathway by using Dilauroyl peroxide (Acros Organics, CAS no. 105-74-8, MW = 398.63 g mol^{-1}), a free radical initiator. The final composition was obtained as follows: 67.5 mg of BBQ and 4 mg of Dilauroyl peroxide were dissolved in 1 mL of vinyl-toluene through ultrasonic stirring. Then hafnia NPs were added to the solution and then dispersed through stirring. The as-prepared solution was placed in a temperature-controlled oil bath at 70 °C for 1 day. For the first 8 h, the mixture was mechanically stirred every hour to avoid nanoparticle sedimentation.

Preparation of Nanocomposites Films: Hundred micrometers polyvinyltoluene films loaded with 10^{-1} M 4,4‴-Bis[(2-butyloctyl)oxy]-1,1′:4′,1″:4″,1‴-quaterphenyl (BBQ) and 2.5%wt. of NPs were prepared as follows: 1 g of composite prepared as discussed in the section above was dissolved in 3 mL of DCM (Sigma Aldrich, CAS no. 75-09-2). Once the solution reached a syrup-like viscosity it was deposited on a glass plate with the help of a doctor blade using a 20 mils blade. The film was then left to air dry until the solvent completely evaporated.

Assembling of Multilayer Scintillators: BGO sheets of size 3 × 3 × 0.1 mm^3 were purchased from EPIC Crystal LTD. They were assembled tighter with 0.1 mm nanocomposite films by hand the multilayer scintillator has been fabricated by alternating BGO and nanocomposite 0.1 mm layers with no glue, in a custom made sample holder, specifically a 3 × 3 × 3 mm^3 Teflon cube with one face open. The internal surfaces had been covered by ESR (Vikuiti) form 3M as reflecting material.

Photoluminescence Studies: Nanoseconds time scale time-resolved photoluminescence experiments had been performed by using as excitation source a pulsed laser LED at 340 nm (3.65 eV, EP-LED 340 Edinburgh Instruments, pulse width 120 ps) and a pulsed laser LED at 250 nm (4.95 eV, EP-LED 250 Edinburgh Instruments, pulse width 77 ps) coupled to FLS980 Edinburgh setup in Time-Correlated Single Photon Counting (TCSPC) acquisition mode. A custom-made 5000M spectrofluorimeter (Horiba Jobin Yvon, Wildwood, MA, USA) equipped with a TBX-04 photon-counting detector (IBH Scotland) and a single grating monochromator was used for PL spectra measurements within 200–800 nm range. As excitation source the laser driven xenon lamp (EQ-99X LDLS Energetic, Hamamatsu Company) was used.

Radioluminescence Studies: Steady state radioluminescence measurements were carried out at room temperature using a liquid nitrogen-cooled charge coupled device (CCD) Symphony II (Jobin-Yvon, Horiba) as a detection system, combined with a monochromator Jobin-Yvon Triax 180 equipped with a 100 lines mm^{-1} grating. For sample excitation, unfiltered X-ray irradiation through a Be window was employed, using a Philips 2274 X-ray tube with tungsten target operated at 20 kV. At this voltage, a continuous X-ray spectrum was produced by a Bremsstrahlung mechanism superimposed to the L and M transition lines of tungsten, due to the impact of electrons generated through thermionic effect and accelerated onto a tungsten target. The dose rate was 5 mGy s^{-1}. All spectra are corrected for the spectral response of the detection system. The nanocomposites LY had been measured by relative methods using the EJ-276-D (LY = 8600 ph MeV^{-1}) plastic scintillator and the inorganic crystal BGO (LY = 10 000 ph MeV^{-1}) as reference (Figure S9, Supporting Information). RL spectra were recorded at cylindrical samples with the same size (1 cm diameter, 0.1 cm thickness) and with similar scattering properties (Figure S10, Supporting Information). All the RL spectra were recorded using a mask with the hole of 0.5 cm in diameter on the sample, a slit width of 0.1 mm and accumulation time 1 s.

X-Rays Scintillation: The scintillation pulses had been recorded in time correlated single photon counting (TCSPC) mode under pulsed X-ray excitation. For this purpose, an X-ray Tube (XRT) N5084 of Hamamatsu was used, activated by a pulsed 405 nm laser (pulse width EP-LED 250 Edinburgh Instruments, pulse width 120 ps). The X-rays energy spectrum was a bremsstrahlung continuous spectrum extending up to 40 keV (as the operating voltage is 40 kV, pulse width 80 ps) with an additional pronounced peak ≈9 keV due to Tungsten L-characteristic X-ray photons. As photodetector, a hybrid photomultiplier tube PMA Hybrid 07 (Picoquant^{GmbH}) coupled to a 4 ps resolution PicoHarp 300 TCSPC module was used. The samples were measured in anti-reflection positioning.

CTR Measurements: The *CTR* under 511 keV was measured with a the setup previously described.[34b] A ^{22}Na radioactive source emits two back-to-back 511 keV gamma photons which are detected by two detectors in coincidence. In the first side a reference crystal LSO:Ce:Ca0.4% of size 2 × 2 × 2 mm^3 (61 ps CTR) was used, while on the other side the sample under investigation was excited. Both scintillators were coupled to a SiPM through Meltmount glue (1.58 refractive index), mounted perpendicularly to the multilayer structure. For the samples under investigation a Broadcom NUV-MT SiPMs biased with 48V (16V overvoltage) was used. The output signals were used as input for an oscilloscope (LeCroy DDA735Zi oscilloscope with 3.5 GHz bandwidth and a sampling rate of 40 Gs s^{-1}), where all information required for the analysis is measured and extracted from the waveforms. The *CTR* values were corrected to compensate the asymmetry of the reference detector.[40]

Radiation/Matter Monte Carlo Simulations: In order to evaluate the energy-sharing effects, a Monte Carlo simulation of the multilayer and bulk scintillators had been performed by means of the FLUKA code.[35] The geometry of the multilayer scintillating heterostructure with a final size of 3 × 3 × 3 mm^3, as well as the two components materials, in terms of atomic weights and density, had been fully reproduced. A the 511 keV photons isotropic source had been put at a distance of 0.5 cm from the scintillator surface. The simulation output had been analyzed on an event-by-event basis through dedicated user-routines developed on purpose. No optical simulation had been performed at this stage.

Light-Propagation Monte Carlo Simulations: Simulations of the scintillator nanocomposite performance were carried out using a home-made Monte Carlo ray-tracing program, in which the photon propagation follows geometrical optics laws and the interference was neglected because of the large nanocomposite dimensions with respect to the light-coherence length. Each scintillation event generates randomly propagating photons whose fate was determined in a stochastic way. In particular, each photon could be absorbed and eventually re-emitted by a chromophore, isotropically scattered, or reflected/ transmitted at the interfaces. The four mirrors placed on the nanocomposite lateral surfaces had been considered with a fixed reflectivity of 95%, independent from the polarization state and from the incidence angle of the light. For the front interfaces with air, Fresnel coefficients were used to compute the reflection probability. The photodetector was coupled to a nanocomposite of dimensions 3 × 3 × 3 mm^3 with an index-matching medium. The photon escape probability from this face was set to unity. The simulated scintillator was the PVT:BBQ:NP*-2.5% specimen. All the considered events (absorption, scattering, transmission or reflection) were chosen according to random Monte Carlo drawing. Simulations were performed using the experimental absorption/luminescence spectrum and emission efficiency (ϕ_{pl} = 0.93) of the chromophore. The system scattering was supposed to give rise to a light attenuation corresponding to an absorption coefficient ranging from 0 to 100 cm^{-1}. Inside the material, for each ray, the inverse transform sampling method was applied for random generation of the length of the optical path before absorption by the chromophores or scattering. Path lengths followed the exponential attenuation law determined by the wavelength-dependent absorption/scattering coefficient. A single-ray-tracing Monte Carlo simulation was repeated 10^6 times. Figure 4c reports the simulated light outcoupling coefficient β calculated for the scintillator detector with fours mirrors placed on the scintillator later faces (inset of Figure 4c) as a function of the scattering level. The β factor decreases as scattering increases from 0.65, for the free-scattering sample, to 0.35, for the sample with the highest simulated scattering level (100 cm^{-1}) When the output-pulse time evolution was computed, the number of iterations was increased to 10^8 to achieve a proper statistical averaging and the output pulse shape was calculated using the following assumptions: 1) the photons were uniformly generated inside the sample or all the scintillation events were generated in fixed positions: close to the front face, close to the rear face, at the center of the sample (Figure 4d); 2) the chromophores are excited promptly by the scintillation. Once a chromophore excited state was generated by scintillation or by re-absorption, the time required to emit a visible photon was determined using the rejection sampling applied to the accurate luminescence decay obtained by the experiment. This time was then added to the time required by the photon to travel to the detector following its own optical path.

Supporting Information

Supporting Information is available from the Wiley Online Library or from the author.

Acknowledgements

M.O. and V.S. contributed equally to this work. This work was carried out in the framework of Crystal Clear Collaboration. The authors acknowledge support from Italian Ministry of University (MUR) through grant PRIN 2020-SHERPA, *Scintillating HEterostructures for High Resolution Fast PET imaging*, no. H45F2100343000 and grant MINERVA - LuMIminesceNt scintillating hEterostructures foR advanced medical imaging no. H25E22000490006. CERN knowledge transfer for medical applications budget. Partial support from EC project Aidainnova, RIA no. 101004761 and Horizon Europe EIC path finder project (Unicorn GA 101098649) is gratefully acknowledged.

Open access publishing facilitated by Universita degli Studi di Milano-Bicocca, as part of the Wiley - CRUI-CARE agreement.

Conflict of Interest

The authors declare no conflict of interest.

Data Availability Statement

All data are available from the authors upon reasonable request.

Keywords

conjugated chromophores, energy transfer, fast scintillators, light yield, nanocomposites, nanoparticles, ToF-PET

Received: November 6, 2024
Revised: December 9, 2024
Published online:

[1] a) P. Lecoq, M. Korznik, presented at 1999 IEEE Nuclear Science Symposium. Conference Record. 1999 Nuclear Science Symposium and Medical Imaging Conference (Cat. No. 99CH37019), Seattle, WA, USA, October **1999**; b) S. Majewski, *Instrum. High Energy Phys.* **1992**, *9*, 157; c) C. Hu, L. Zhang, R.-Y. Zhu, *J. Phys. Conf. Ser.* **2022**, *2374*, 012110; d) C. Dujardin, E. Auffray, E. Bourret-Courchesne, P. Dorenbos, P. Lecoq, M. Nikl, A. N. Vasil'ev, A. Yoshikawa, R. Y. Zhu, *IEEE Trans. Nucl. Sci.* **2018**, *65*, 1977.

[2] CERN, European Community for Future Accellerators 2021 (https://indico.cern.ch/event/957057/page/23281-the-roadmap-document (accessed: February 2024).
[3] a) M. Conti, B. J. C. Bendriem, *Clin. Transl. Imaging* **2019**, *7*, 139; b) D. R. J. P. M. Schaart, *Biology* **2021**, *66*, 09TR01; c) A. Wibowo, M. A. K. Sheikh, L. J. Diguna, M. B. Ananda, M. A. Marsudi, A. Arramel, S. Zeng, L. J. Wong, M. D. Birowosuto, *Commun. Mater.* **2023**, *4*, 21; d) P. Lecoq, C. Morel, J. O. Prior, D. Visvikis, S. Gundacker, E. Auffray, P. Križan, R. M. Turtos, D. Thers, E. Charbon, J. Varela, C. de La Taille, A. Rivetti, D. Breton, J.-F. Pratte, J. Nuyts, S. Surti, S. Vandenberghe, P. Marsden, K. Parodi, J. M. Benlloch, M. Benoit, *Phys. Med. Biol.* **2020**, *65*, 21RM01.
[4] a) R. M. Turtos, S. Gundacker, E. Auffray, P. Lecoq, *Phys. Med. Biol.* **2019**, *64*, 185018; b) M. Orfano, F. Pagano, I. Mattei, F. Cova, V. Secchi, S. Bracco, E. Rogers, L. Barbieri, R. Lorenzi, G. Bizarri, E. Auffray, A. Monguzzi, *Adv. Mater. Technol.* **2024**, *9*, 2302075; c) P. Krause, E. Rogers, G. Bizarri, *Adv. Theory Simul.* **2024**, *7*, 2300425.
[5] a) E. G. Rogers, M. D. Birowosuto, F. Maddalena, C. Dujardin, F. Pagano, N. Kratochwil, E. Auffray, P. Krause, G. Bizarri, *Appl. Phys. Lett.* **2023**, *122*, 081901; b) F. Pagano, J. Král, K. Děcká, M. Pizzichemi, E. Mihóková, V. Čuba, E. Auffray, *Adv. Mater. Interfaces* **2024**, *11*, 2300659; c) F. Pagano, N. Kratochwil, M. Salomoni, M. Pizzichemi, M. Paganoni, E. Auffray, *Phys. Med. Biol.* **2022**, *67*, 135010.
[6] O. Kilicoglu, E. E. Altunsoy, O. Agar, M. Kamislioglu, M. I. Sayyed, H. O. Tekin, N. Tarhan, *Results Phys.* **2019**, *14*, 102424.
[7] Eljen Technology, https://eljentechnology.com/products/plastic-scintillators.
[8] a) G. H. V. Bertrand, F. Sguerra, C. Dehé-Pittance, F. Carrel, R. Coulon, S. Normand, E. Barat, T. Dautremer, T. Montagu, M. Hamel, *J. Mater. Chem. C* **2014**, *2*, 7304; b) G. H. V. Bertrand, J. Dumazert, F. Sguerra, R. Coulon, G. Corre, M. Hamel, *J. Mater. Chem. C* **2015**, *3*, 6006; c) U. Shirwadkar, E. Van Loef, G. Markosyan, M. McClish, J. Glodo, K. Shah, presented at 2015 IEEE Nuclear Science Symposium and Medical Imaging Conference (NSS/MIC), San Diego, CA, USA, October **2015**; d) M. Koshimizu, G. H. V. Bertrand, M. Hamel, S. Kishimoto, R. Haruki, F. Nishikido, T. Yanagida, Y. Fujimoto, K. Asai, *Jpn. J. Appl. Phys.* **2015**, *54*, 102202; e) M. J. Ford, E. Aigeldinger, F. Sutanto, N. P. Zaitseva, V. A. Li, M. L. Carman, A. Glenn, C. Roca, S. A. Dazeley, N. Bowden, *Nucl. Instrum. Methods Phys. Res., Sect. A* **2023**, *1050*, 168093; f) F. Cova, A. Erroi, M. L. Zaffalon, A. Cemmi, I. Di Sarcina, J. Perego, A. Monguzzi, A. Comotti, F. Rossi, F. Carulli, S. Brovelli, *Nano Lett.* **2024**, *24*, 905.
[9] a) T. J. Hajagos, C. Liu, N. J. Cherepy, Q. Pei, *Adv. Mater.* **2018**, *30*, 1706956; b) H. Zhao, H. Yu, C. Redding, Z. Li, T. Chen, Y. Meng, T. J. Hajagos, J. P. Hayward, Q. Pei, *ACS Appl. Nano Mater.* **2021**, *4*, 1220; c) M. Gandini, I. Villa, M. Beretta, C. Gotti, M. Imran, F. Carulli, E. Fantuzzi, M. Sassi, M. Zaffalon, C. Brofferio, L. Manna, L. Beverina, A. Vedda, M. Fasoli, L. Gironi, S. Brovelli, *Nat. Nanotechnol.* **2020**, *15*, 462; d) M. Orfano, J. Perego, F. Cova, C. X. Bezuidenhout, S. Piva, C. Dujardin, B. Sabot, S. Pierre, P. Mai, C. Daniel, S. Bracco, A. Vedda, A. Comotti, A. Monguzzi, *Nat. Photonics* **2023**, *17*, 672; e) K. Rajakrishna, A. Dhanasekaran, N. Yuvaraj, K. C. Ajoy, B. Venkatraman, M. T. Jose, *Nucl. Instrum. Methods Phys. Res., Sect. A* **2021**, *1008*, 165454; f) V. S. Shevelev, A. V. Ishchenko, A. S. Vanetsev, V. Nagirnyi, S. I. Omelkov, *J. Lumin.* **2022**, *242*, 118534; g) F. Hiyama, T. Noguchi, M. Koshimizu, S. Kishimoto, R. Haruki, F. Nishikido, Y. Fujimoto, T. Aida, S. Takami, T. Adschiri, K. Asai, *Jpn. J. Appl. Phys.* **2018**, *57*, 052203; h) C. Frangville, A. Grabowski, J. Dumazert, E. Montbarbon, C. Lynde, R. Coulon, A. Venerosy, G. H. V. Bertrand, M. Hamel, *Nucl. Instrum. Methods Phys. Res., Sect. A* **2019**, *942*, 162370; i) M. Koshimizu, *Funct. Mater. Lett.* **2020**, *13*, 2030003; j) M. Koshimizu, in *Plastic Scintillators: Chemistry and Applications*, (Ed: M. Hamel), Springer International Publishing, Cham **2021**, p. 201.
[10] G. H. V. Bertrand, M. Hamel, in *Plastic Scintillators: Chemistry and Applications*, (Ed: M. Hamel), Springer International Publishing, Cham **2021**, p. 139.
[11] I. Villa, A. Monguzzi, R. Lorenzi, M. Orfano, V. Babin, F. Hájek, K. Kuldová, R. Kučerková, A. Beitlerová, I. Mattei, H. Buresova, R. Pjatkan, V. Čuba, L. Prouzová Procházková, M. Nikl, *Nano Lett.* **2024**, *24*, 8248.
[12] a) C. Liu, T. J. Hajagos, D. Kishpaugh, Y. Jin, W. Hu, Q. Chen, Q. Pei, *Adv. Funct. Mater.* **2015**, *25*, 4607; b) I. Villa, F. Moretti, M. Fasoli, A. Rossi, B. Hattendorf, C. Dujardin, M. Niederberger, A. Vedda, A. Lauria, *Adv. Opt. Mater.* **2020**, *8*, 1901348.
[13] J. S. Reddin, J. S. Scheuermann, D. Bharkhada, A. M. Smith, M. E. Casey, M. Conti, J. S. Karp, presented at 2018 Ieee nuclear science symposium and medical imaging conference proceedings (Nss/Mic), Sydney, NSW, Australia, November **2018**.
[14] E. Luxottica, (https://exciton.luxottica.com/laser-dyes.html.
[15] a) A. F. Adadurov, D. A. Yelyseev, V. D. Titskaya, V. N. Lebedev, P. N. Zhmurin, *Radiat. Meas.* **2011**, *46*, 498; b) P. de Sainte Claire, *J. Phys. Chem. B* **2006**, *110*, 7334; c) M. S. Healy, J. E. Hanson, *J. Appl. Polym. Sci.* **2007**, *104*, 360.
[16] I. Villa, B. Santiago Gonzalez, M. Orfano, F. Cova, V. Secchi, C. Colombo, J. Páterek, R. Kučerková, V. Babin, M. Mauri, M. Nikl, A. Monguzzi, *Nanomaterials* **2021**, *11*, 3387.
[17] S. M. Woodley, S. Hamad, J. A. Mejías, C. R. A. Catlow, *J. Mater. Chem.* **2006**, *16*, 1927.
[18] D. Muñoz Ramo, J. L. Gavartin, A. L. Shluger, G. Bersuker, *Phys. Rev. B* **2007**, *75*, 205336.
[19] A. Veved, G. W. Ejuh, N. Djongyang, *Polym. Bull.* **2021**, *78*, 4977.
[20] V. Kiisk, S. Lange, K. Utt, T. Tätte, H. Mändar, I. Sildos, *Phys. B* **2010**, *405*, 758.
[21] T. V. Perevalov, V. S. Aliev, V. A. Gritsenko, A. A. Saraev, V. V. Kaichev, E. V. Ivanova, M. V. Zamoryanskaya, *Appl. Phys. Lett.* **2014**, *104*, 071904.
[22] V. A. Gritsenko, T. V. Perevalov, D. R. Islamov, *Phys. Rep.* **2016**, *613*, 1.
[23] B. Cojocaru, D. Avram, R. Negrea, C. Ghica, V. G. Kessler, G. A. Seisenbaeva, V. I. Parvulescu, C. Tiseanu, *ACS Omega* **2019**, *4*, 8881.
[24] I. Villa, L. P. Procházková, E. Mihóková, V. Babin, R. Král, P. Zemenová, A. Falvey, V. Čuba, M. Salomoni, F. Pagano, R. Calà, I. Frank, E. Auffray, M. Nikl, *CrystEngComm* **2023**, *25*, 4345.
[25] M. Kirm, J. Aarik, M. Jürgens, I. Sildos, *Nucl. Instrum. Methods Phys. Res., Sect. A* **2005**, *537*, 251.
[26] D. Muñoz Ramo, P. V. Sushko, A. L. Shluger, *Phys. Rev. B* **2012**, *85*, 024120.
[27] S. Tagawa, N. Nakashima, K. J. M. Yoshihara, *Macromolecules* **1984**, *17*, 1167.
[28] R. D. Burkhart, G. W. Haggquist, S. E. J. M. Webber, *Macromolecules* **1987**, *20*, 3012.
[29] a) S. Vinogradov, *Nucl. Instrum. Methods Phys. Res., Sect. A* **2018**, *912*, 149; b) E. Auffray, B. Frisch, F. Geraci, A. Ghezzi, S. Gundacker, H. Hillemanns, P. Jarron, T. Meyer, M. Paganoni, K. Pauwels, M. Pizzichemi, P. Lecoq, *IEEE Trans. Nucl. Sci.* **2013**, *60*, 3163; c) S. Gundacker, R. Martinez Turtos, N. Kratochwil, R. H. Pots, M. Paganoni, P. Lecoq, E. Auffray, *Phys. Med. Biol.* **2020**, *65*, 025001.
[30] F. Pagano, N. Kratochwil, L. Martinazzoli, C. Lowis, M. Paganoni, M. PIzzichemi, E. Auffray, *IEEE Trans. Nucl. Sci.* **2023**, *70*, 2630.
[31] J. A. Bearden, *Rev. Mod. Phys.* **1967**, *39*, 78.
[32] J. Perego, I. Villa, A. Pedrini, E. C. Padovani, R. Crapanzano, A. Vedda, C. Dujardin, C. X. Bezuidenhout, S. Bracco, P. E. Sozzani, A. Comotti, L. Gironi, M. Beretta, M. Salomoni, N. Kratochwil, S. Gundacker, E. Auffray, F. Meinardi, A. Monguzzi, *Nat. Photonics* **2021**, *15*, 393.
[33] a) M. Ishii, K. Harada, Y. Hirose, N. Senguttuvan, M. Kobayashi, I. Yamaga, H. Ueno, K. Miwa, F. Shiji, F. Yiting, M. Nikl, X. Q. Feng, *Opt. Mater.* **2002**, *19*, 201; b) R. Cala', N. Kratochwil, L. Martinazzoli,

M. T. Lucchini, S. Gundacker, E. Galenin, I. Gerasymov, O. Sidletskiy, M. Nikl, E. Auffray, *Nucl. Instrum. Methods Phys. Res., Sect. A* **2022**, *1032*, 166527; c) F. Pagano, N. Kratochwil, I. Frank, S. Gundacker, M. Paganoni, M. Pizzichemi, M. Salomoni, E. Auffray, *Front. Phys.* **2022**, *10*, 1021787.

[34] a) M. Kapusta, J. Pawelke, M. Moszyński, *Nucl. Instrum. Methods Phys. Res., Sect. A* **1998**, *404*, 413; b) S. Gundacker, R. M. Turtos, E. Auffray, M. Paganoni, P. Lecoq, *Phys. Med. Biol.* **2019**, *64*, 055012.

[35] a) A. Ferrari, J. Ranft, P. R. Sala, A. Fassò, *FLUKA: A multi-particle transport code*, CERN, Geneva, **2005**; b) T. T. Böhlen, F. Cerutti, M. P. W. Chin, A. Fassò, A. Ferrari, P. G. Ortega, A. Mairani, P. R. Sala, G. Smirnov, V. Vlachoudis, *Nucl. Data Sheets* **2014**, *120*, 211.

[36] S. Surti, A. Kuhn, M. E. Werner, A. E. Perkins, J. Kolthammer, J. S. Karp, *J. Nucl. Med.* **2007**, *48*, 471.

[37] R. M. Turtos, S. Gundacker, S. Omelkov, B. Mahler, A. H. Khan, J. Saaring, Z. Meng, A. Vasil'ev, C. Dujardin, M. Kirm, I. Moreels, E. Auffray, P. Lecoq, *npj 2D Mater. Appl.* **2019**, *3*, 37.

[38] Y. Wan, X. Zhou, *RSC Adv.* **2017**, *7*, 7763.

[39] I. Villa, A. Vedda, M. Fasoli, R. Lorenzi, N. Kränzlin, F. Rechberger, G. Ilari, D. Primc, B. Hattendorf, F. J. Heiligtag, M. Niederberger, A. Lauria, *Chem. Mater.* **2016**, *28*, 3245.

[40] F. Pagano, N. Kratochwil, C. Lowis, W.-S. Choong, M. Paganoni, M. Pizzichemi, J. W. Cates, E. Auffray, *Phys. Med. Biol.* **2024**, *69*, 205012.